J Nanopart Res (2018) 20: 279
https://doi.org/10.1007/s11051-018-4359-3

RESEARCH PAPER

Facile synthesis of recyclable Co_3O_4/$Co(OH)_2$/RGO ternary heterostructures with synergistic effect for photocatalysis

Haiyan Li · Cheng Sun · Yan Zhao · Xingjian Xu · Hongwen Yu

Received: 7 January 2018 / Accepted: 10 September 2018 / Published online: 19 October 2018

Abstract A simple one-pot hydrothermal approach has been provided for the synthesis of a magnetically recyclable Co_3O_4/$Co(OH)_2$/RGO ternary visible-light photocatalyst. The chemical reduction of graphene oxide (GO) and the formation of Co_3O_4 and $Co(OH)_2$ nanoparticles occurred simultaneously during the hydrothermal reaction, and an intimate interface is built successfully between $Co(OH)_2$ and Co_3O_4 nanoparticles at the nanoscale. The formation mechanism of Co_3O_4/$Co(OH)_2$/RGO is investigated by means of TEM and XRD, indicating that the RGO nanosheets play a vital role in forming the ternary heterostructures. The synergistic effect between Co_3O_4, $Co(OH)_2$, and RGO leads to decreased aggregation of nanoparticles, more surface active sites, two electron-transfer paths, and excellent charge transfer. As a result, a highly efficient and stable photocatalytic activity is obtained for the 6-wt% Co_3O_4/$Co(OH)_2$/RGO ternary heterojunction photocatalyst under visible-light illumination ($\lambda >$ 420 nm). Furthermore, the photocatalyst can be rapidly collected from the suspension using a powerful magnet and recycled with good stability, which is very meaningful in the practical industry and life.

H. Li · C. Sun · Y. Zhao · H. Yu (✉)
School of Life Science and Technology, Changchun University of Science and Technology, Changchun 130022, China
e-mail: yuhw@iga.ac.cn

X. Xu · H. Yu
Key Laboratory of Wetland Ecology and Environment, Northeast Institute of Geography and Agroecology, Chinese Academy of Sciences, Changchun 130102, China

Keywords Ternary heterostructure · Visible light · Magnetically recyclable · Nanostructured photocatalyst · Environmental effects

Introduction

Heterogeneous photocatalysis using semiconductor materials and solar energy offers an ideal green approach to the solution of serious energy shortages and environmental problems, where an active semiconductor material is undoubtedly an important key (O'Regan and Gratzel 1991; Hoffmann et al. 1995; Sushma and Girish Kumar 2017). To date, TiO_2, with excellent performance, has long been the focus of semiconductor material. However, the wide band gap (E_g = 3.2 eV) and high recombination probability of photogenerated carriers have limited its practical application (Anpo and Takeuchi 2003; Choi et al. 1994). Compared with the conventional TiO_2 photocatalyst, more attention has been paid to Cobalt-based oxides and hydroxide (e.g., Co_3O_4 and $Co(OH)_2$) among the various transition-metal oxides (Li et al. 2015). Especially, Co_3O_4 has attracted increasing interest as a visible-light photocatalyst, because of its good sunlight utilization (E_g = 2.1 eV), remarkable oxidation ability (2.76 V vs. NHE), magnetic property, nontoxicity, chemical stability, and low cost (Zhang et al. 2014a, b). However, the serious aggregation and poor photoelectric conversion property of Co_3O_4 lead to low photocatalytic degradation activity; therefore, how to overcome the above

disadvantages and improve the photocatalytic activity of Co_3O_4 is an urgent issue.

Recently, researchers found that the construction and preparation of semiconductor-heterojunction photocatalysts could effectively improve its photocatalytic activity, because the heterojunction with matched energy band gaps could form the internal in-built electric fields and provide a potential driving force to enhance the separation of photogenerated charge carriers, and restrain its recombination (Yu et al. 2008; Chen et al. 2005; Xiang et al. 2012). Generally, the semiconductor-heterojunction photocatalysts are mainly divided into the following four types: (1) the semiconductor/semiconductor heterojunction; (2) the metal/semiconductor heterojunction; (3) the carbon-based materials/semiconductor heterojunction (carbon-based materials mainly include the carbon nanotube and graphene); (4) the multicomponent heterojunction (Wang et al. 2014). The multicomponent heterojunction, which is composed of two or more semiconductor materials and an electronic transmission system, can effectively improve the utilization of solar light and drive separation and transportation of the photogenerated charge carriers. Among the various electronic transmission systems, graphene appears to be an ideal candidate, and its excellent electronic conductivity could enhance the separation efficiency of photogenerated charge carriers in the graphene-based nanocomposites. Moreover, graphene is also an attractive support material for the deposition and dispersion of nanoparticles due to its lamellar structure and high specific surface, leading to high photocatalytic activity (Zhang et al. 2010a; Lightcap et al. 2010). However, up to now, the synthesis of multicomponent heterojunction, in which cobalt oxides, cobalt hydroxide and graphene are spatially integrated, has never been reported. So, design and preparation of efficient and separable visible-light-driven Co_3O_4/$Co(OH)_2$/RGO photocatalytic heterojunction, which conform to the needs of practical industry and life, is very meaningful and the aim of this study.

In this work, we report for the fabrication of a ternary heterojunction photocatalyst (Co_3O_4/$Co(OH)_2$/RGO) integrated Co_3O_4, $Co(OH)_2$ and reduced graphene oxide (RGO) through a simple one-pot hydrothermal approach. It is worth mentioning that the chemical reduction of graphene oxide (GO) and construction of Co_3O_4 and $Co(OH)_2$ heterojunction operated at the same time during hydrothermal process, and RGO nanosheet plays a vital role in forming the heterojunction. The as-prepared Co_3O_4 and $Co(OH)_2$ nanoparticles are scattered on the RGO nanosheet surface to avoid magnetic agglomeration of Co_3O_4 nanoparticles as well as the restacking of RGO nanosheets. The novel ternary heterojunction photocatalyst combine the merits of each component: Both Co_3O_4 and $Co(OH)_2$ nanoparticles as visible-light-active photocatalysts can convert solar light into photogenerated electron-hole pairs, RGO nanosheets are used as electron collectors to transfer the photogenerated electrons from semiconductor photocatalyst, while magnetic Co_3O_4 nanoparticles are used to rapidly collect and recover photocatalysts using a powerful magnet. As expected, the as-prepared Co_3O_4/$Co(OH)_2$/RGO ternary heterojunction photocatalyst exhibits higher catalytic ability in photodegradation of Congo red (CR) dyestuff, due to the synergistic effect between Co_3O_4, $Co(OH)_2$, and RGO.

Experimental section

Preparation of GO

GO was prepared from natural graphite powder through a modified Hummers' method (Hummers Jr and Offeman 1958; Li et al. 2012; Lu et al. 2011).

Preparation of Co_3O_4/$Co(OH)_2$/RGO ternary heterojunction photocatalyst

A series of ternary Co_3O_4/$Co(OH)_2$/RGO heterojunction photocatalysts with varying GO adding amounts were prepared by a hydrothermal process and labeled as x wt% Co_3O_4/$Co(OH)_2$/RGO (x wt% is the weight ratio of GO to the resulting products). A certain amount of GO and 0.2 g of CTAB were dispersed in the mixture of distilled water (10 mL) and absolute ethanol (50 mL) with the aid of ultrasonication. Subsequently, 0.08 g of NaOH and 0.1455 g of $Co(NO_3)\cdot 6H_2O$ were added into the above suspension, respectively. After magnetic stirring for 2 h, the suspension (pH 14) was loaded into a 100 mL of hydrothermal autoclave and kept the temperature at 160 °C for 4 h in an electric oven. After cooling to room temperature, the sample in autoclave was collected by high-speed centrifugation, then, washed with ethanol and water alternatively for several times until pH 7. Finally, the sample was dried at 50 °C for 24 h in an oven before characterization.

Preparation of Co_3O_4, $Co(OH)_2$, RGO, $Co(OH)_2$/RGO, Co_3O_4/$Co(OH)_2$, and Co_3O_4/RGO photocatalysts

For control experiments, pure Co_3O_4 and β-$Co(OH)_2$ samples were also prepared according to the previous report (Liang et al. 2006). 0.5 g of $Co(CH_3COO)_2{\cdot}4H_2O$ was dissolved in the mixture of ethylene glycol (20 mL) and distilled water (0.4 mL), after microwave heating at 170 °C for 5 min; the cobalt acetate hydroxide precursor was obtained by centrifugation. Finally, the precursor was redispersed in 20 mL of distilled water and microwave heated at 100 °C for 20 min to obtain the β-$Co(OH)_2$ sample. The pure Co_3O_4 was obtained by a hydrothermal method using the above cobalt acetate hydroxide precursor. The precursor was dispersed in 20 mL of distilled water, then, 1 mL of H_2O_2 (1 mol/L) was added, and the suspension was loaded into a 40 mL of hydrothermal autoclave and kept the temperature at 140 °C for 12 h to obtain the Co_3O_4 sample.

RGO was prepared through a facile hydrothermal treatment. GO was dispersed in the mixture of distilled water (60 mL) and absolute ethanol (30 mL) with the aid of ultrasonication, then, the suspension was loaded into a hydrothermal autoclave and kept the temperature at 120 °C for 10 h in an electric oven.

The $Co(OH)_2$/RGO, Co_3O_4/$Co(OH)_2$, and Co_3O_4/RGO composite photocatalysts were prepared by mixing the two corresponding powders at the desired ratio.

Characterizations

The crystal structure of ternary Co_3O_4/$Co(OH)_2$/RGO heterojunction photocatalysts was characterized with the X-ray diffraction (XRD, Rigaku D/Max-2550) and Raman spectrometer (J-Y T64000). Its morphology and structure was measured on transmission electron micrographs (TEM, HITACHI H-8100 EM) and scanning electron microscopy (SEM, XL30 ESEM FEG). Photoluminescence (PL) spectra were recorded on a microplate reader (BioTek Synergy H1M) with the excitation wavelength of 320 nm. Thermogravimetric analysis (TGA) was operated on a TGA 4000 analyzer (PerkinElemer) in air, controlling the temperature from 30–900 °C with a rate of 10 °C/min. The UV-vis diffuse reflectance spectra were recorded with a Shimadzu 3600 UV-vis-NIR spectrophotometer equipped with an integrating sphere diffuse reflectance accessory, while $BaSO_4$ was used as a reference. The total organic carbon (TOC) analysis was measured with a total organic carbon analyzer (TOC/L CPH).

Photoelectrochemical measurements

All the electrochemical measurements (transient photocurrents, current-voltage (*I-V*), electrochemical impedance spectroscopy (EIS)) were performed by using a CHI 660D electrochemical analyzer (CH Instruments, Shanghai), and a homemade three-electrode cell composed of a saturated calomel electrode, a platinum wire, and the as-prepared photocatalysts as the reference, counter, and working electrodes, respectively, and a 1-M NaOH solution was used as the electrolyte. The transient photocurrents were carried out using a 500-W xenon lamp (CHFXQ500W, Beijing) with a cutoff filter ($\lambda > 420$ nm). Electrochemical impedance spectroscopy (EIS) measurements were conducted in the frequency range from 100 kHz to 0.01 Hz at open circuit potential with an AC perturbation of 5 mV.

Photocatalytic test

The photocatalytic activity test is carried out in a set of photocatalytic devices purchased from Beijing Perfectlight Co. Ltd., which mainly includes the following three sections: (1) Pyrex reaction cell fitted with cooling-water interlayer and a quartz cover is used as a reactor; (2) Low-temperature thermostat bath (BILOW-W-501) is used to control the temperature of a photocatalytic reactor at 20 °C; (3) Xenon lamp (PLS-SXE300C, 500 W) fitted with an optical band-pass filter is used as a solar-light source to simulate visible light ($\lambda > 420$ nm). In a typical test, 0.05 g of ternary Co_3O_4/$Co(OH)_2$/RGO heterojunction was first dispersed in 50 mL of 100 mg L^{-1} CR aqueous solution, and kept stirring in the dark for 60 min. After reaching the adsorption-desorption balance, the system was simulated with Xenon lamp, and the photodegradation efficiency of CR was monitored on a UV-vis spectrophotometer (PE, Lambda 25) in real time.

Active species test

The main active species during the photocatalytic process were detected by the scavenging experiments, p-benzoquinone (BQ, 0.0001 mol/L), disodium ethylenediaminetetraacetate (EDTA, 0.01 mol/L) and isopropanol (IPA, 0.01 mol/L) were used as $\cdot O_2^-$

radicals, h^+, and $^{\cdot}OH$ radicals scavenger, respectively. The scavengers were added to the CR solution prior to irradiation in three separated systems.

Results and discussion

Morphology of Co_3O_4/$Co(OH)_2$/RGO ternary heterojunction

The morphology of obtained products was first monitored through the TEM, as shown in Fig. 1. Figure 1 shows TEM images of the as-prepared samples; Fig. 1a displays the well-dispersed GO nanosheets with many wrinkles. After the hydrothermal reaction of GO with $Co(NO_3)\cdot 6H_2O$, obviously, a large amount of nanoparticles with diameter at the range of 8 to 23 nm are scattered on the nanosheets surface (Fig. 1b, c). The HRTEM image in Fig. 1e and its corresponding electron diffraction pattern (Fig. 1d) suggest that the nanoparticles are highly crystallized; the measured interlayer spacing of 0.47 nm is same as the distance of (111) crystallographic planes of Co_3O_4 with a face-centered cubic structures (Nie et al. 2013) and that of 0.24 nm consistent with the (002) crystallographic planes of β-$Co(OH)_2$ (Li et al. 2015; Zhou et al. 2016; Koza et al. 2013). These observations indicate that an intimate interface is built successfully between $Co(OH)_2$ and Co_3O_4 nanoparticles at the nanoscale, and RGO as a support material avoids the agglomeration of Co_3O_4 and $Co(OH)_2$ nanoparticles, making more surface active positions to participate in the photocatalytic process. For comparison, the 6-wt% Co_3O_4/$Co(OH)_2$/RGO ternary heterojunction photocatalyst without CTAB was also prepared, and its TEM and HRTEM images were shown in Fig. 1f, g. An intimate interface of $Co(OH)_2$ and Co_3O_4 nanoparticles is also observed; however, it is obviously that the RGO has a poor dispersion, indicating that the CTAB can play a role in dispersing GO nanosheets.

Structural analysis

The crystalline nature of the as-prepared samples was examined by X-ray diffraction (XRD) analysis, as shown in Fig. 2. Figure 2a shows the XRD patterns of the as-prepared samples with different hydrothermal temperature, at a lower reaction temperature of 100 °C and 120 °C; the main peaks, around 19.0°, 31.3°, 36.9°, 38.5°, 44.8°, 59.4°, and 65.2°, can be indexed to the (111), (220), (311), (222), (400), (511), and (440) planes of Co_3O_4 with face-centered cubic structures (JCDPDS no. 42-1467). In contrast, when the reaction temperature increased to 160 °C, the sample exhibits that additional peaks at 32.5°, 37.9°, 51.4°, 57.9°, and 59.6° can be indexed to the (100), (101), (102), (110), and (003) planes of β-$Co(OH)_2$ phase with a hexagonal structure (JCDPDS no. 30-0443), indicating that the mixed-crystalline phases of Co_3O_4 and β-$Co(OH)_2$ form under these reaction conditions (Li et al. 2015). Moreover, the crystallization degree of sample is further improved as reaction temperature increased to 180 °C. In the next work, we choose 160 °C as the reaction temperature to explore the effect of reaction time on the crystal phase of products, as shown in Fig. 2b. At a shorter reaction time of 2 h, only the face-centered cubic Co_3O_4 phase is obtained. However, when the reaction time is prolonged to 4 h, the diffraction peaks of β-$Co(OH)_2$ phase with a hexagonal structure are observed besides Co_3O_4. Similarly, the crystallization degree of products is further improved as reaction time increased from 4 to 12 h. Figure 2c compares the XRD patterns of samples prepared at 160 °C for 4 h with different pH. The pH of precursor solution is adjusted by NaOH from 6.2 to 14; it is clearly seen that single face-centered cubic Co_3O_4 phase is obtained, when the pH is 6.2. When the pH increases from 8.6 to 14, both Co_3O_4 and β-$Co(OH)_2$ phases are obtained. In contrast, the pH of precursor solution is adjusted to 11.6 using $NH_3\cdot H_2O$ instead of NaOH, but only face-centered cubic Co_3O_4 phase is produced. Based on the above results, we continue to explore the influence of GO adding amounts on the crystal phase of products prepared at 160 °C for 4 h, and pH 14. Without addition of GO, the diffraction peaks for 0-wt% sample can be ascribed to the well-crystallized Co_3O_4 with face-centered cubic structures, which is consistent with the above results of TEM images. After adding GO in the system, the diffraction peaks of β-$Co(OH)_2$ phase with a hexagonal structure are observed besides Co_3O_4. In addition, the XRD peak of RGO nanosheets at approximately 26° is absent; this phenomenon may be due to the low amount of GO introduced in the system, or the weak peak intensity of RGO disguised by that of others, leading it invisible.

Based on the above XRD results, we assume that the GO nanosheets play a vital role in forming the ternary Co_3O_4/$Co(OH)_2$/RGO heterojunction. During the hydrothermal process, $Co(NO_3)_2\cdot 6H_2O$ is used as Co precursor, the hydration and hydrolysis reactions of Co^{2+} will occur to

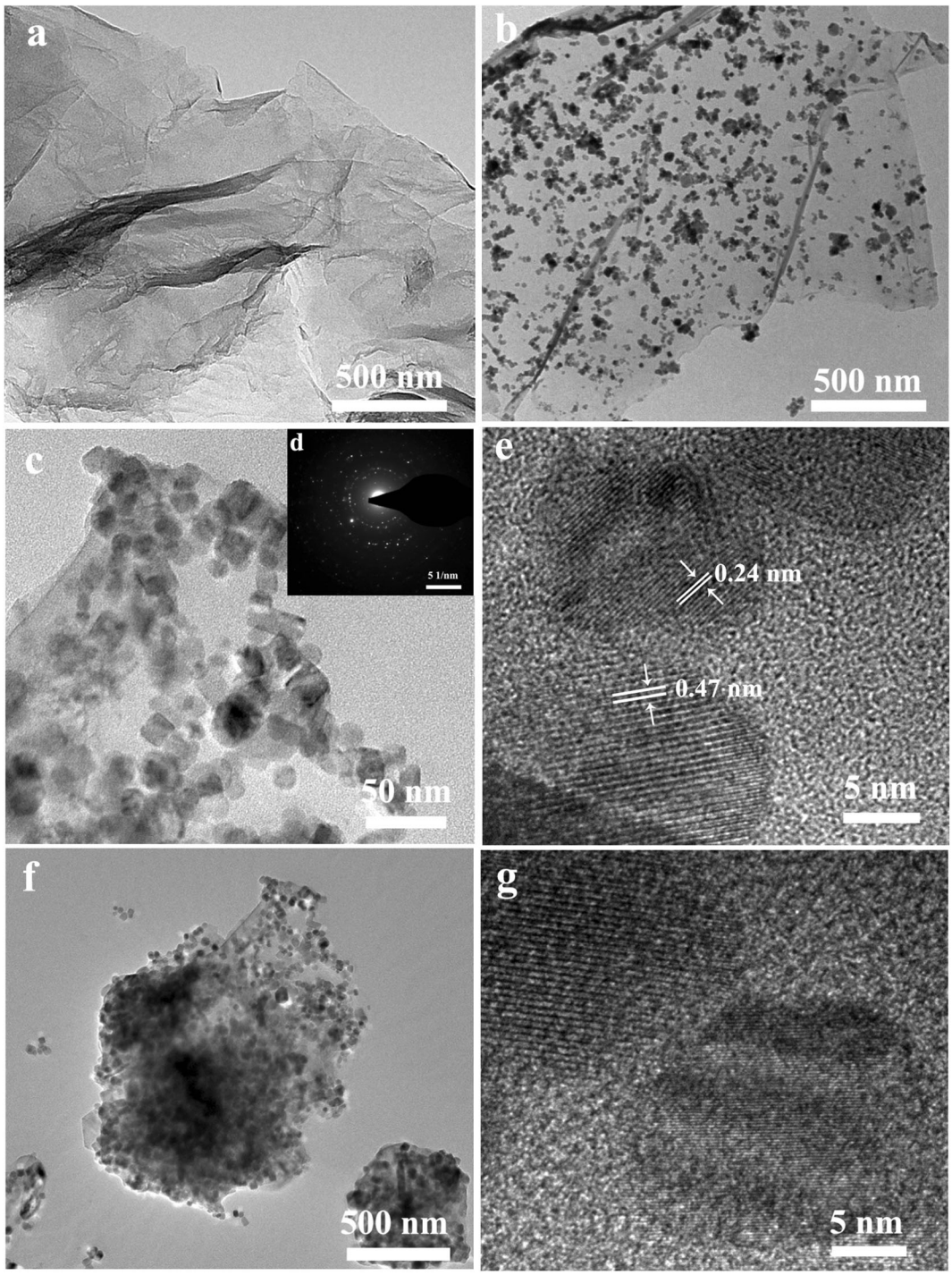

Fig. 1 (**a**) TEM image of GO, (**b**) low, (**c**) high magnification TEM images, (**d**) electron diffraction pattern, and (**e**) HRTEM image of the as-prepared 6-wt% $Co_3O_4/Co(OH)_2$/RGO ternary heterojunction photocatalyst with CTAB. (**f**) TEM and (**g**) HRTEM images of 6-wt% $Co_3O_4/Co(OH)_2$/RGO ternary heterojunction photocatalyst without CTAB

generate the hydroxo complex of Co^{2+} ($[Co(OH)_4]^{2-}$), and some $[Co(OH)_4]^{2-}$ will be further oxidized and transformed into the hydroxo complex of Co^{3+} ($[Co(OH)_6]^{3-}$) with an increase of the system temperature and pressure. Finally, the

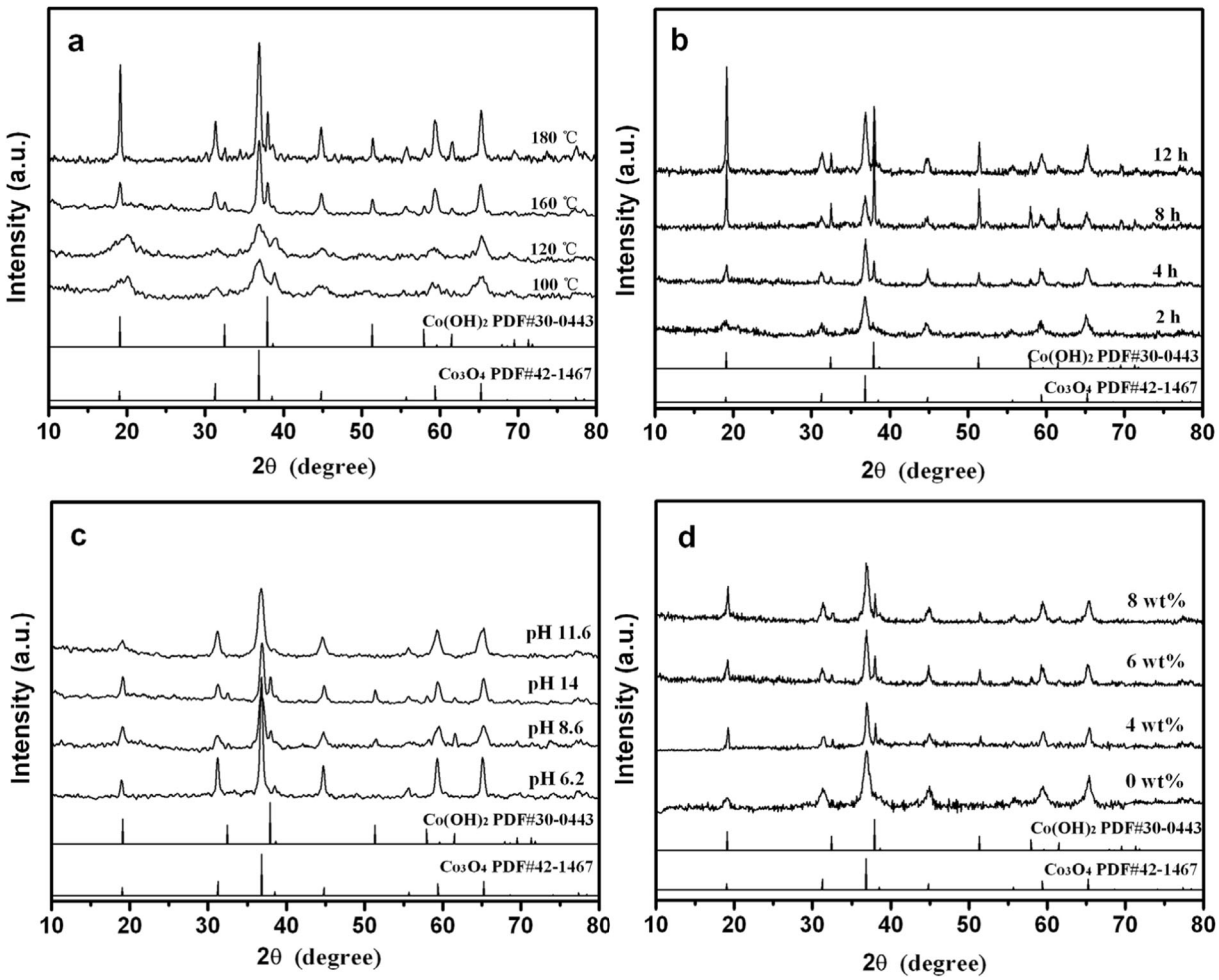

Fig. 2 X-ray diffraction spectra of the as-prepared samples with (a) different hydrothermal temperature, reaction conditions: the amount of GO, 6 wt%; reaction time, 4 h; pH 14, (b) different reaction time, reaction conditions: the amount of GO, 6 wt%; reaction temperature, 160 °C; pH 14, (c) different pH, reaction conditions: the amount of GO, 6 wt%; reaction temperature, 160 °C; reaction time, 4 h, and (d) different GO adding amounts, reaction conditions: reaction temperature, 160 °C; reaction time, 4 h; pH 14

Co_3O_4 formed through the fasciculation reaction of $[Co(OH)_4]^{2-}$ and $[Co(OH)_6]^{3-}$ with a mole ratio of 1:2. However, the mole ratio of $[Co(OH)_4]^{2-}$ and $[Co(OH)_6]^{3-}$ is above 1:2, due to the introduction of GO in this system, leading some $Co(OH)_2$ obtained through the fasciculation reaction of $[Co(OH)_4]^{2-}$. Thus, the ternary Co_3O_4/$Co(OH)_2$/RGO heterojunction photocatalysts are obtained by a simple one-pot hydrothermal method.

The successful one-pot reduction of GO and the formation of $Co(OH)_2$ and Co_3O_4 were also verified by Raman spectroscopy. Figure 3 shows the Raman spectra of GO and 6-wt% Co_3O_4/$Co(OH)_2$/RGO ternary heterojunction. For GO, there are two obvious peaks at ~ 1355 (D-band) and ~ 1601 cm^{-1} (G-band). After the hydrothermal reaction, it is obvious that the as-prepared sample shows relative higher intensity ratio of D to G-band ($I_D/I_G = 0.98$) than that of GO (0.82), indicating the reduction of GO during the hydrothermal reaction (Chen and Yan 2010). In addition, other peaks at approximately 485, 524, 692, and 1127 cm^{-1} are detected, which are consistent with the reported E_{2g}, $2F_{2g}$, and $A1_g$ phonon modes of Co_3O_4 and the OH deformation modes of β-$Co(OH)_2$, respectively (Liu and Patzke 2014; Abd El-sadek et al. 2010; Yang et al. 2010). All the above characterization results further proved that the chemical reduction of GO and the formation of Co_3O_4 and $Co(OH)_2$ nanoparticles occurred simultaneously during one-pot hydrothermal process.

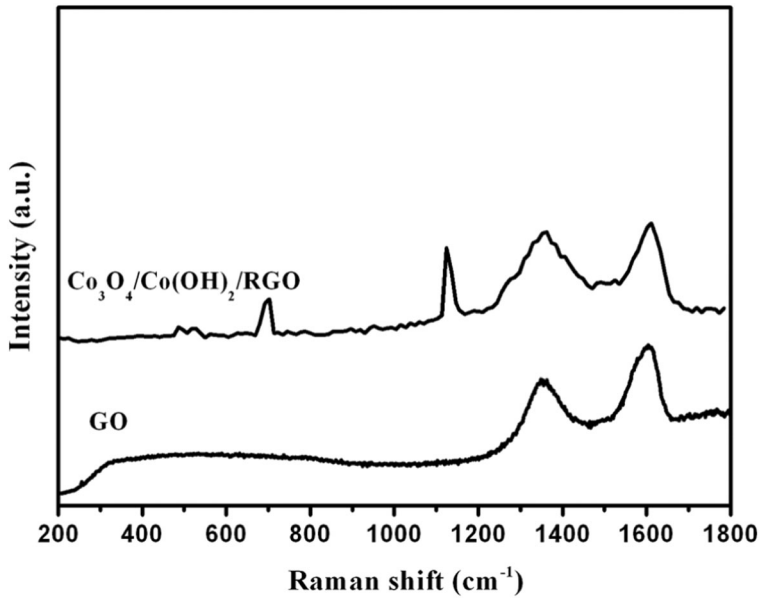

Fig. 3 Raman spectra of GO and the 6-wt% $Co_3O_4/Co(OH)_2$/RGO ternary heterojunction

In order to obtain the content information of $Co(OH)_2$, Co_3O_4 in the $Co_3O_4/Co(OH)_2$/RGO ternary heterojunction, thermogravimetric analysis (TGA) was used to characterize the samples, as shown in Fig. 4. For the $Co_3O_4/Co(OH)_2$/RGO ternary heterojunction, the mass loss (~ 2 wt%) below 100 °C is caused by the loss of adsorbed water from sample (Wang et al. 2011). There are two rapid mass loss at 200–400 °C and 400–700 °C, the former is attributed to the thermal decomposition of $Co(OH)_2$ into Co_3O_4, and the latter is attributed to the combustion of carbon skeleton of RGO nanosheets (Li et al. 2010). According to the TGA results, we can calculate that the content of $Co(OH)_2$, Co_3O_4, and RGO is ~ 7 wt%, 85 wt%, and 6 wt%, respectively. The calculated content of RGO is consistent with the adding amount of RGO.

Optical absorption characteristic

The optical absorption characteristic is an important parameter to evaluate photocatalytic performance of

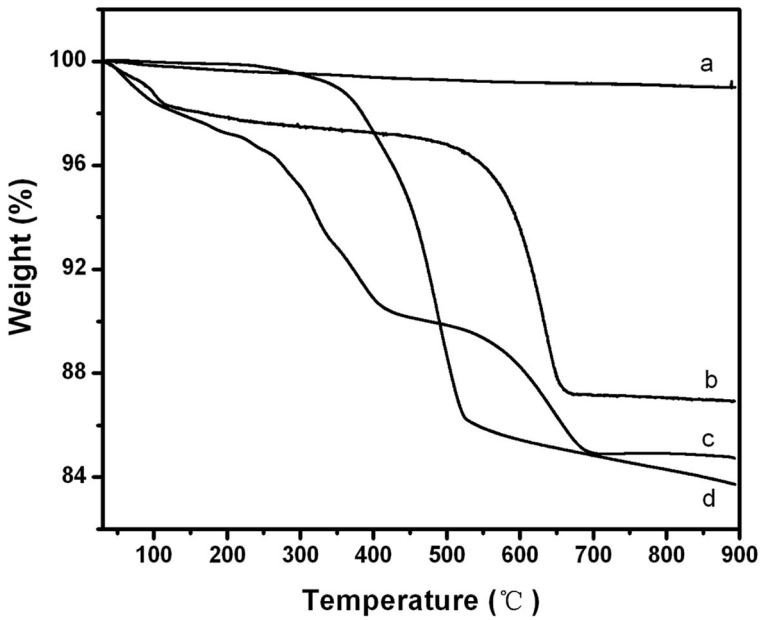

Fig. 4 TGA curves of (**a**) pure Co_3O_4, (**b**) Co_3O_4/RGO, (**c**) 6-wt% $Co_3O_4/Co(OH)_2$/RGO ternary heterojunction, and (**d**) pure $Co(OH)_2$

semiconductors. Figure 5 shows the UV-vis diffuse reflectance spectra of pure $Co(OH)_2$, Co_3O_4, and $Co_3O_4/Co(OH)_2$/RGO ternary heterojunction. The pure $Co(OH)_2$ shows an obvious visible-light absorption (400–700 nm), which is ascribed to the d-d transition of Co(II) (Zhang et al. 2014a). The pure Co_3O_4 shows a single broad absorption band across the entire range (200–800 nm), which is the $O \rightarrow Co^{2+}$ charge transfer, d-d transition of Co^{2+} and Co^{3+} (Liu and Patzke 2014). For the $Co_3O_4/Co(OH)_2$/RGO ternary heterojunction, their absorption curves are similar to those of pure Co_3O_4 because of the higher content of Co_3O_4 in ternary heterojunction.

Photocatalytic activity of $Co_3O_4/Co(OH)_2$/RGO ternary heterojunction

Congo red (CR), a benzidine-based, direct, anionic diazo dyestuff, is mainly used as dyeing agent for cotton, hemp, silk, and other textile products to give a red color. The effluents containing CR dyestuff are highly colored, resulting in major environmental problems. Thus, we choose CR as the target dyestuff to evaluate the visible-light photocatalytic activity of ternary $Co_3O_4/Co(OH)_2$/RGO heterojunction. Figure 6a compares the kinetics of photodegradation of CR by using pure $Co(OH)_2$, Co_3O_4, 6-wt% $Co(OH)_2$/RGO, $Co_3O_4/Co(OH)_2$, 6-wt% Co_3O_4/RGO, and ternary $Co_3O_4/Co(OH)_2$/RGO photocatalysts with varying amounts of RGO. Obviously, the decomposition of CR is negligible in the absence

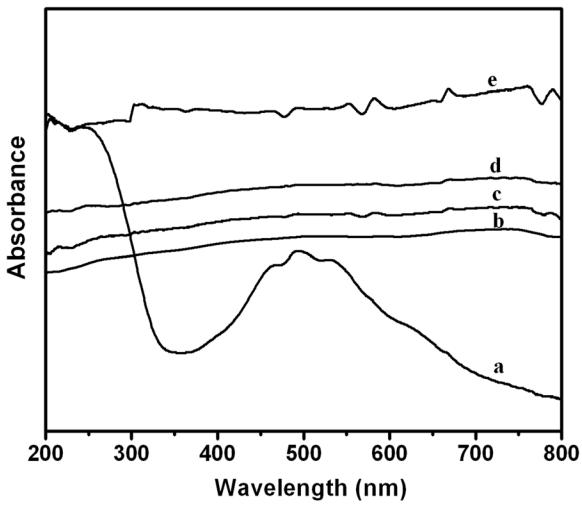

Fig. 5 UV-vis diffuse reflectance spectra of pure (**a**) $Co(OH)_2$, (**e**) Co_3O_4 and $Co_3O_4/Co(OH)_2$/RGO ternary heterojunction with varying GO adding amounts, (**b**) 4 wt%, (**c**) 6 wt%, (**d**) 8 wt%

of photocatalyst in the control experiment. For comparison, the photocatalytic activity of pure $Co(OH)_2$ and Co_3O_4, 6 wt% $Co(OH)_2$/RGO, 6 wt% Co_3O_4/RGO, and $Co_3O_4/Co(OH)_2$ are also checked, and about 15%, 27%, 20%, 10%, and 37% of CR, respectively, had been degraded under the same testing conditions. However, it is obvious that the $Co_3O_4/Co(OH)_2$/RGO ternary heterojunction shows significant improvement of photodegradation efficiency of CR compared to the above photocatalysts, and about 73%, 90%, and 63% are eliminated from the solution within 60 min in the presence of 4%, 6%, and 8% $Co_3O_4/Co(OH)_2$/RGO ternary heterojunction photocatalysts, indicating the presence of synergistic effect between Co_3O_4, $Co(OH)_2$, and RGO in photocatalytic reaction. The highest photocatalytic efficiency was obtained from 6% $Co_3O_4/Co(OH)_2$/RGO as 90%; when the RGO content is increased to 8%, the photocatalytic activity is reduced, indicating that there is an optimal value for the adding amount of RGO. When the RGO content is lower than 6%, the photogenerated electrons in ternary heterojunction cannot be effectively transferred by a small amount of RGO. When the RGO content is higher than 6%, a large amount of RGO will directly affect the incident light transmittance of photocatalyst, preventing the generation of photoinduced electron-hole pairs in the photocatalyst.

In addition, the UV-vis absorption spectra of CR, the TOC content, and CR removal efficiency at different irradiation times using 6-wt% $Co_3O_4/Co(OH)_2$/RGO ternary heterojunction photocatalyst during the photocatalytic process were recorded and shown in Fig. 6b, c. As the illumination time is prolonged, the absorption intensity of CR aqueous solution gradually decreased, but, the maximum absorption wavelength of CR aqueous solution keeps at 496 nm, and no new absorbance peaks are observed. Furthermore, it can be seen that the CR removal efficiency dramatically decreases in the first 60 min, and reaches 99% after 150 min. Correspondingly, the TOC content shows a similar trend, and the TOC removal efficiency reaches 95% after 150 min (Fig. 6c), indicating that the CR dyestuff has been completely degraded, and the photocatalytic activity of $Co_3O_4/Co(OH)_2$/RGO ternary heterojunction is better than that of many previous reports on Cobalt-based photocatalysts (Bin and Hui 2015; Shi et al. 2012). Moreover, according to the kinetic study results in Fig. 6d, the photodegradation process of CR complies with pseudo-first-order kinetics, and the 6-wt% Co_3O_4/

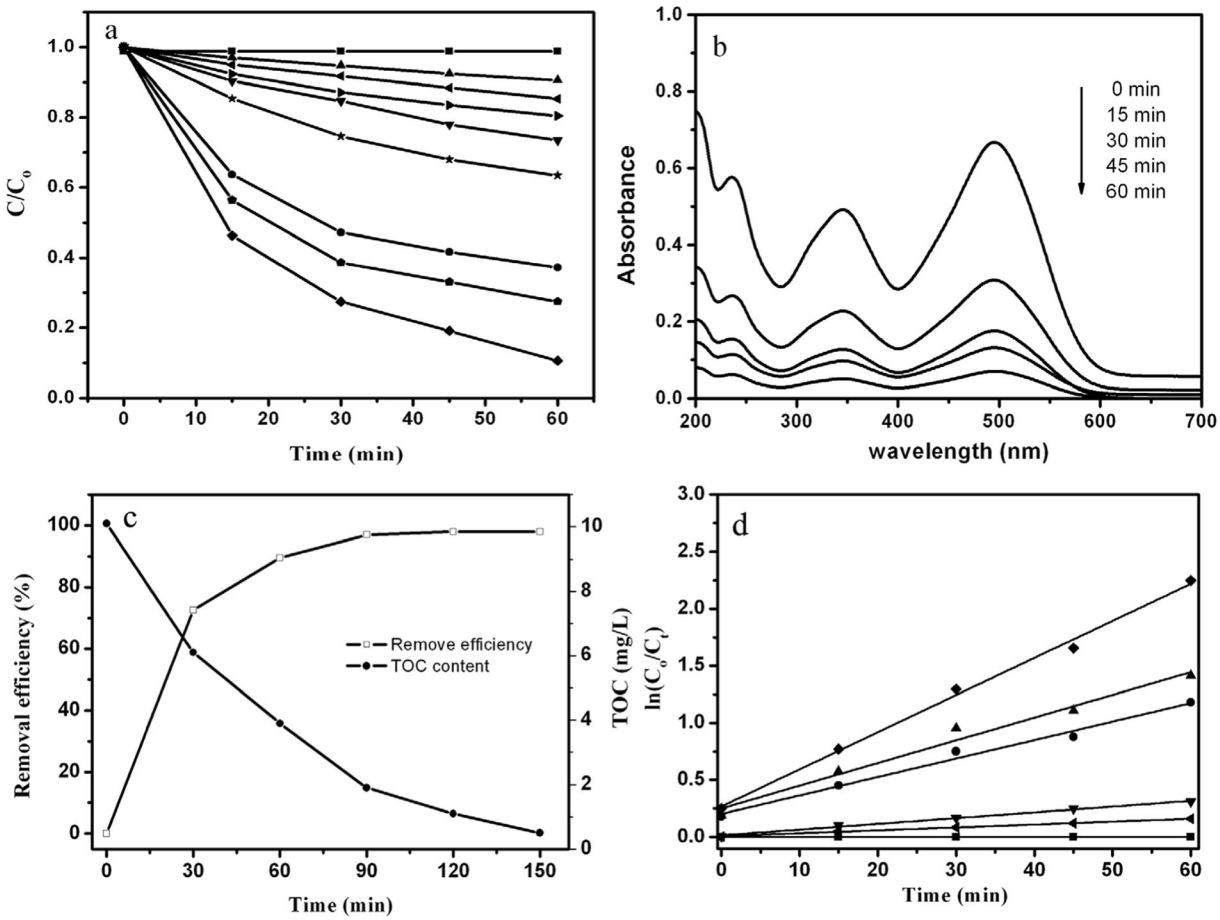

Fig. 6 (**a**) The kinetics of photodegradation of CR (■) by using pure $Co(OH)_2$ (◀), pure Co_3O_4 (▼), 6-wt% $Co(OH)_2$/RGO (▶), 6-wt% Co_3O_4/RGO (▲), Co_3O_4/$Co(OH)_2$ (), and Co_3O_4/$Co(OH)_2$/RGO ternary heterojunction with different amounts of RGO (● = 4 wt%; = 6 wt%; ♦= 8 wt%). (**b**) UV-vis absorption spectra of CR using 6-wt% Co_3O_4/$Co(OH)_2$/RGO ternary heterojunction photocatalyst under visible light ($\lambda > 420$ nm). (**c**) The TOC content and CR removal efficiency at different irradiation times using 6% Co_3O_4/$Co(OH)_2$/RGO ternary heterojunction photocatalysts. (**d**) Kinetic fit for the photodegradation of CR (■) by using pure $Co(OH)_2$ (◀), Co_3O_4 (▼), and Co_3O_4/$Co(OH)_2$/RGO ternary heterojunction with different amounts of RGO (●= 4 wt%; ♦= 6 wt%; ▲ = 8 wt%)

$Co(OH)_2$/RGO ternary heterojunction shows a higher kinetic constant (0.0329 min^{-1}) than others (Table 1).

Recycling ability is also an important factor to estimate the photocatalyst performance besides the photocatalytic efficiency, and Fig. 7a shows the recycling photocatalytic test of 6-wt% $Co(OH)_2$/RGO, Co_3O_4/RGO, and Co_3O_4/$Co(OH)_2$/RGO ternary heterojunction photocatalyst. Obviously, there is no significant change in photocatalytic activity during the five cycles, implying that a good stability of $Co(OH)_2$/RGO, Co_3O_4/RGO, and ternary Co_3O_4/$Co(OH)_2$/RGO photocatalysts. Moreover, the ternary heterojunction can be rapidly collected from the suspension using a powerful magnet, as shown in Fig. 7b, which is very meaningful in the practical industry and life applications. Thus, all above-mentioned results indicate that

Table 1 Pseudo-first-order rate constants and R^2 of different photocatalysts photodegraded on CR

Photocatalyst	k (min^{-1})	R^2
No photocatalyst	1.349×10^{-5}	0.99013
Pure $Co(OH)_2$	0.0025	0.9984
Pure Co_3O_4	0.0050	0.9971
4-wt% Co_3O_4/$Co(OH)_2$/RGO	0.0162	0.9939
6-wt% Co_3O_4/$Co(OH)_2$/RGO	0.0329	0.9977
8-wt% Co_3O_4/$Co(OH)_2$/RGO	0.0199	0.9904

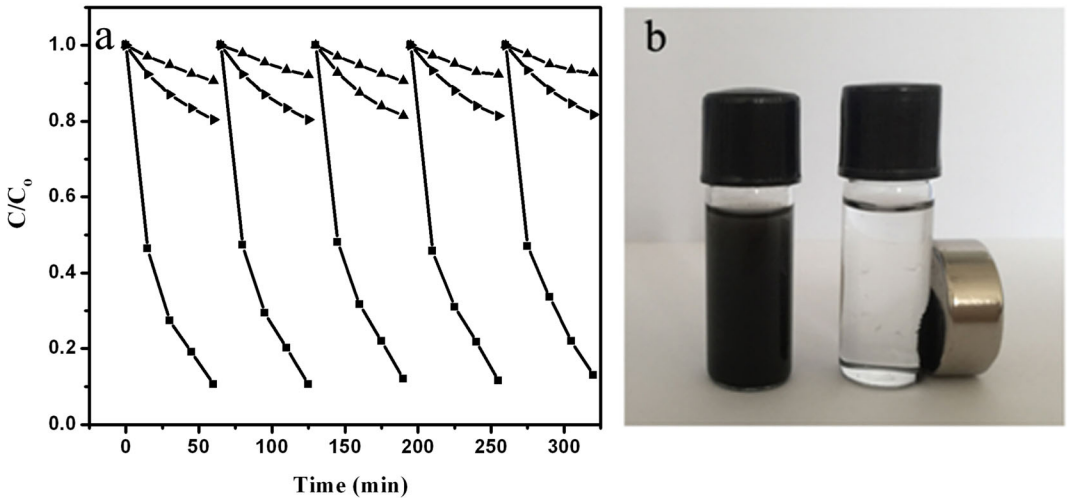

Fig. 7 (**a**) Recycling photocatalytic test of 6-wt% $Co(OH)_2$/RGO (►), 6-wt% Co_3O_4/RGO (▲), and 6-wt% Co_3O_4/$Co(OH)_2$/RGO (♦) ternary heterojunction photocatalyst, (**b**) a digital photo illustrates the separation process of ternary heterojunction from the suspension by using a powerful magnet

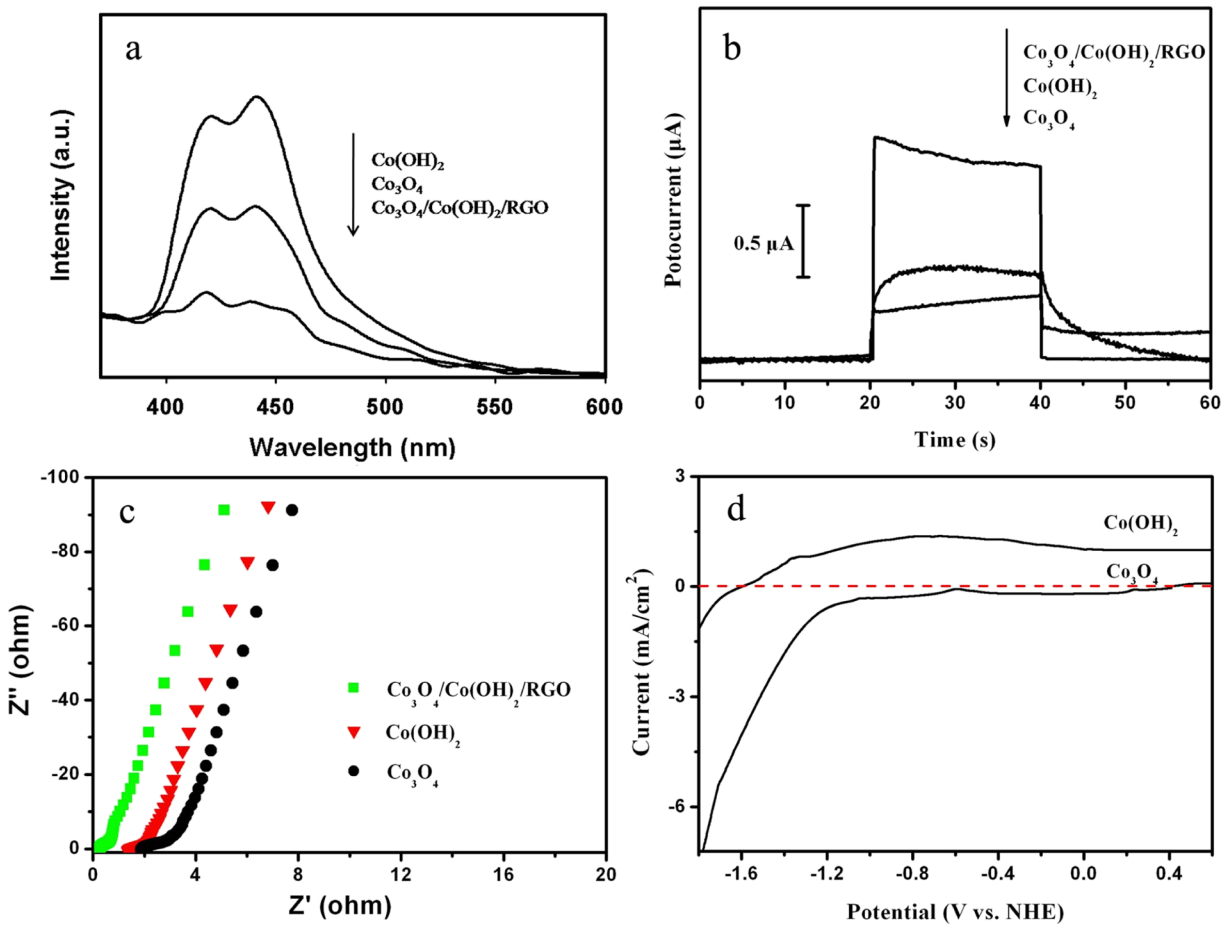

Fig. 8 (a) Photoluminescence spectra, (b) transient photocurrents, (c) EIS Nyquist plots, and (d) *I-V* characteristics of pure $Co(OH)_2$, Co_3O_4, and 6-wt% Co_3O_4/$Co(OH)_2$/RGO ternary heterojunction

the Co_3O_4/$Co(OH)_2$/RGO ternary heterojunction is a promising candidate for photocatalysts in practical application.

Synergistic effect of Co_3O_4/$Co(OH)_2$/RGO ternary heterojunction

The photoluminescence (PL) spectrum is an effective means to investigate the microscopic behavior of photoinduced charge in semiconductor, including generation, transmission, and recombination, because the PL emission is derived from the recombination of photoinduced electron-hole pairs. Figure 8a compares the PL spectra of pure $Co(OH)_2$, Co_3O_4, and 6-wt% Co_3O_4/$Co(OH)_2$/RGO ternary heterojunction; there is a broad band in range 380–600 nm for all the samples. Obviously, the emission intensity of 6-wt% Co_3O_4/$Co(OH)_2$/RGO ternary heterojunction is much weaker than that of pure $Co(OH)_2$ and Co_3O_4, indicating a high charge-separation rate (Wu et al. 2015; Hou et al. 2013).

The transient photocurrent of ternary Co_3O_4/$Co(OH)_2$/RGO photocatalyst under irradiation with visible light ($\lambda > 420$ nm) for 20 s is shown in Fig. 8b. As can be seen, the pure Co_3O_4 (0.43 μA) and $Co(OH)_2$ (0.64 μA) show a small anodic photocurrent, which means that the photogenerated electrons move to the bulk and subsequently transfer to the ITO electrode, leaving holes on the outer surface. However, compared with the pure Co_3O_4 and $Co(OH)_2$, a significant enhancement in the photocurrent is observed for ternary Co_3O_4/$Co(OH)_2$/RGO photocatalyst (1.5 μA), indicating that the synergistic effect between Co_3O_4, $Co(OH)_2$, and RGO can enhance the separation of charge carriers.

Figure 8c shows the EIS Nyquist plots of pure $Co(OH)_2$, Co_3O_4, and 6-wt% Co_3O_4/$Co(OH)_2$/RGO ternary heterojunction. Generally, the smaller arc in an EIS Nyquist plot indicates a smaller charge-transfer resistance on the electrode surface (Lim et al. 2014). The Co_3O_4/$Co(OH)_2$/RGO ternary heterojunction shows a relative smaller arc size than that of pure $Co(OH)_2$ and Co_3O_4, manifesting the higher efficiency of charge separation and transfer. The above experimental results indicate that the ternary heterojunction could significantly improve the separation of photoinduced electron-hole pairs and restrain its recombination, which is very beneficial to improve the photocatalytic activity.

Photocatalytic mechanism of Co_3O_4/$Co(OH)_2$/RGO ternary heterojunction

The main active species during the photocatalytic process were detected by the scavenging experiments, as shown in Fig. 9a. The photocatalytic degradation of CR is slightly inhibited in the presence of EDTA (h^+ scavenger), while it is intensively suppressed by the addition of IPA ($^{\cdot}OH$ scavenger) or p-BQ ($^{\cdot}O_2^-$ scavenger) into this system. Thus, it can be inferred that the main active species affect the photocatalytic activity in the following order: $^{\cdot}OH > {}^{\cdot}O_2^- > h^+$.

The flat band potentials of photocatalysts were recorded by the *I-V* test (Fig. 8d). The flat band potential

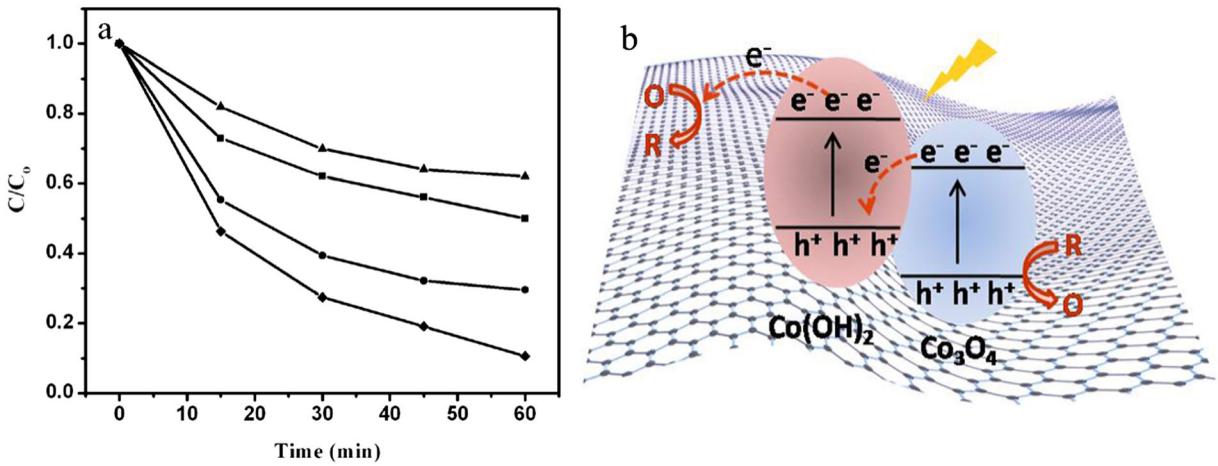

Fig. 9 (**a**) Photocatalytic activity of the 6-wt% Co_3O_4/$Co(OH)_2$/RGO ternary heterojunction for degradation of CR in the presence of different scavengers, EDTA (●), p-BQ (■), IPA (▲), and no scavenger (♦). (**b**) Microscopic mechanism of the Co_3O_4/$Co(OH)_2$/RGO ternary heterojunction during the photocatalytic process

represents the apparent Fermi level of a semiconductor in equilibrium with a redox couple, and the Fermi level lies close to the conduction band (CB) of the n-type semiconductor (Zhang et al. 2010a, b). The pure $Co(OH)_2$ and Co_3O_4 show flat potential at − 1.60 V and 0.42 V vs NHE, according to the band gap energy of $Co(OH)_2$ ($E_g = 2.9$ eV) and Co_3O_4 ($E_g = 2.1$ eV); the calculated valence band (VB) is 1.30 V and 1.68 V vs NHE for pure $Co(OH)_2$ and Co_3O_4, respectively.

We analyzed the test results mentioned above, and concluded the operating of Z-scheme charge carrier mechanism in the $Co_3O_4/Co(OH)_2$/RGO ternary structure (Fig. 9b). According to the band theory of semiconductors, both $Co(OH)_2$ and Co_3O_4 are visible-light active components; they can be excited simultaneously, using the visible light ($\lambda > 420$ nm). Their photogenerated electrons can be transferred from each VB to CB. On the one hand, some electrons in the CB of Co_3O_4 easily transfer to the VB of $Co(OH)_2$ (electron transfer path I) and recombine with the holes (Maeda et al. 2016). On the other hand, other electrons in the CB of $Co(OH)_2$ can transfer to the Fermi level of graphene (0 V vs. NHE) (electron transfer path II) that is an excellent electron conductor (Iwase et al. 2011; Hayashi et al. 2011). The processes of electron transfer paths I and II could effectively enhance the separation of photogenerated charge carriers and restrain its recombination. As a result, a lot of photogenerated electrons on graphene and $Co(OH)_2$ nanoparticles surface as well as holes on Co_3O_4 nanoparticles surface that participate in the photocatalytic reactions can directly and indirectly decompose CR dye, respectively. Thus, the ternary $Co_3O_4/Co(OH)_2$/RGO heterojunction photocatalyst could exhibit a better photocatalytic activity.

Conclusions

In conclusion, ternary $Co_3O_4/Co(OH)_2$/RGO heterojunction photocatalysts were constructed by a simple one-step synthetic strategy, and the RGO plays a vital role in constructing the ternary heterojunction. The obtained ternary $Co_3O_4/Co(OH)_2$/RGO heterojunction showed an excellent photocatalytic performance stimulated by visible light, which should be contributed to the cooperative effects and cooperation of two aspects: (1) RGO as a support material avoids the agglomeration of Co_3O_4 and $Co(OH)_2$ nanoparticles, making more surface active positions to participate in the photocatalytic process; (2) The synergistic effect between Co_3O_4, $Co(OH)_2$, and RGO enhance the separation of photogenerated charge carriers and restrain its recombination. Furthermore, the ternary $Co_3O_4/Co(OH)_2$/RGO heterojunction photocatalysts can be rapidly collected from the suspension using a powerful magnet and recycled with good stability, which is very meaningful in the practical industry and life. So, this research makes sense to construct graphene-based multicomponent nanocomposites for photocatalysis and other applications.

Funding information The research was supported by the National Key R&D Program of China (2017YFC0505901), the "Hundred Talents project" of the Chinese Academy of Science, 135 Breading Project of Chinese Academy of Sciences (Northeast Institute of Geography and Agroecology, no. Y6H2081001), the Excellent Young Scientists Foundation of the Northeast Institute of Geography and Agroecology (DLSYQ14001), and the Project of Science and Technology Development Plan of Jilin Province (no. 20160520025JH), the financial support of the Education Department of Jilin province "13th Five-Year" Science and Technology Research project [grant number 2016-382], and the Youth Science Foundation of Changchun University of Science and Technology University [grant number XQNJJ-2016-07].

Compliance with ethical standards

Conflict of interest The authors declare that they have no conflict of interest.

References

Abd El-sadek MS, Ram Kumar J, Moorthy Babu S, Salim El-Hamidy M (2010) Aqueous synthesis and characterization of CdTe@$Co(OH)_2$ (core–shell) composite nanoparticles. Mater Chem Phys 124(1):592–599

Anpo M, Takeuchi M (2003) The design and development of highly reactive titanium oxide photocatalysts operating under visible light irradiation. J Catal 216:505–516

Bin Z, Hui L (2015) Three-dimensional porous graphene-Co_3O_4 nanocomposites for high performance photocatalysts. Appl Sur Sci 357:439–444

Chen JL, Yan XP (2010) A dehydration and stabilizer free approach to production of stable water dispersions of graphene nanosheets. J Mater Chem 20(21):4328–4332

Chen YS, Crittenden JC, Hackney S, Sutter L, Hand DW (2005) Preparation of a novel TiO_2-based p−n junction nanotube photocatalyst. Environ Sci Technol 39(5):1201–1208

Choi W, Termin A, Hoffmann MR (1994) The role of metal ion dopants in quantum-sized TiO_2: correlation between photoreactivity and charge carrier recombination dynamics. J Phys Chem 98:13669–13679

Hayashi H, Lightcap IV, Tsujimoto M, Takano M, Umeyama T, Kamat PV, Imahori H (2011) Electron transfer cascade by organic/inorganic ternary composites of porphyrin, zinc oxide nanoparticles, and reduced graphene oxide on a tin oxide electrode that exhibits efficient photocurrent generation. J Am Chem Soc 133(20):7684–7687

Hoffmann MR, Martin ST, Choi WY, Bahnemannt DW (1995) Environmental applications of semiconductor photocatalysis. Chem Rev 95:69–96

Hou JG, Yang C, Wang Z, Zhou WL, Jiao SQ, Zhu HM (2013) In situ synthesis of α–β phase heterojunction on Bi_2O_3 nanowires with exceptional visible-light photocatalytic performance. Appl Catal B Environ 142:504–511

Hummers WS Jr, Offeman R (1958) Preparation of graphitic oxide. J Am Chem Soc 80(6):1339–1339

Iwase A, Ng YH, Ishiguro Y, Kudo A, Amal R (2011) Reduced graphene oxide as a solid-state electron mediator in Z-scheme photocatalytic water splitting under visible light. J Am Chem Soc 133(29):11054–11057

Koza JA, Hull CM, Liu YC, Switzer JA (2013) Deposition of beta-$Co(OH)_2$ films by electrochemical reduction of tris(ethylenediamine)cobalt(III) in alkaline solution. Chem Mater 25(9):1922–1926

Li HY, Liu S, Tian JQ, Wang L, Lu WB, Luo YL, Asiri A, Al-Youbi A, Sun XP (2012) Ternary nanocomposites of porphyrin, angular Au nanoparticles and reduced graphene oxide: photocatalytic synthesis and enhanced photocurrent generation. ChemCatChem 4:1079–1083

Li N, Wang ZY, Zhao KK, Shi ZJ, Gu ZN, Xu SK (2010) Large scale synthesis of N-doped multi-layered graphene sheets by simple arc-discharge method. Carbon 48(1):255–259

Li W, Li PT, Liu Y, Zhang BL, Zhang HP, Geng WC, Zhang QY (2015) Efficient photocatalytic degradation of dyes over hierarchical BiOBr/β-$Co(OH)_2$/PVP multicomponent photocatalyst under visible-light irradiation. ChemCatChem 7(24):4163–4172

Liang ZH, Zhu YJ, Cheng GF, Huang YH (2006) Microwave-assisted synthesis of β-$Co(OH)_2$ and Co_3O_4 nanosheets via a layered precursor conversion method. Can J Chem 84:1050–1053

Lightcap IV, Kosel TH, Kamat PV (2010) Anchoring semiconductor and metal nanoparticles on a two-dimensional catalyst mat. Storing and shuttling electrons with reduced graphene oxide. Nano Lett 10:577–583

Lim J, Monllor-Satocaa D, Jang JS, Lee S, Choi W (2014) Visible light photocatalysis of fullerol-complexed TiO_2 enhanced by Nb doping. Appl Catal B Environ 152–153:233–240

Liu HF, Patzke GR (2014) Visible-light-driven water oxidation with nanoscale Co_3O_4: new optimization strategies. Chem Asian J 9(8):2249–2259

Lu WB, Chang GH, Luo YL, Liao F, Sun XP (2011) Method for effective immobilization of Ag nanoparticles/graphene oxide composites on single-stranded DNA modified gold electrode for enzyme less H_2O_2 detection. J Mater Sci 46:5260–5266

Maeda K, Ishimaki K, Tokunaga Y, Lu DL, Eguchi M (2016) Modification of wide-band-gap oxide semiconductors with cobalt hydroxide nanoclusters for visible-light water oxidation. Angew Chem Int Ed 55(29):8309–8313

Nie RF, Shi JJ, Du WC, Ning WS, Hou ZY, Xiao FS (2013) A sandwich N-doped graphene/Co_3O_4 hybrid: an efficient catalyst for selective oxidation of olefins and alcohols. J Mater Chem A 1(32):9037–9045

O'Regan B, Gratzel M (1991) A low-cost, high-efficiency solar cell based on dye-sensitized colloidal titanium dioxide films. Nature 353(6346):737–740

Shi PH, Su RJ, Wan FZ, Zhu MC, Li DX, Xu SH (2012) Co_3O_4 nanocrystals on graphene oxide as a synergistic catalyst for degradation of Orange II in water by advanced oxidation technology based on sulfate radicals. Appl Catal B Environ 123–124:265–272

Sushma C, Girish Kumar S (2017) Advancements in the zinc oxide nanomaterials for efficient photocatalysis. Chem Pap 71(10):2023–2042

Wang HL, Zhang LS, Chen ZG, Hu JQ, Li SJ, Wang ZH, Liu JS, Wang XC (2014) Semiconductor heterojunction photocatalysts: design, construction, and photocatalytic performances. Chem Soc Rev 43(15):5234–5244

Wang SY, Yu DS, Dai LM, Chang DW, Baek JB (2011) Polyelectrolyte-functionalized graphene as metal-free electrocatalysts for oxygen reduction. ACS Nano 5(8): 6202–6209

Wu M, Yan JM, Zhang XW, Zhao M, Jiang Q (2015) Ag_2O modified g-C_3N_4 for highly efficient photocatalytic hydrogen generation under visible light irradiation. J Mater Chem A 3(30):15710–15714

Xiang QJ, Yu JG, Jaroniec M (2012) Graphene-based semiconductor photocatalysts. Chem Soc Rev 41(2):782–796

Yang J, Liu HW, Martens WN, Frost RL (2010) Synthesis and characterization of cobalt hydroxide, cobalt oxyhydroxide, and cobalt oxide nanodiscs. J Phys Chem C 114(1):111–119

Yu HB, Chen S, Quan X, Zhao HM, Zhang YB (2008) Fabrication of a TiO_2−BDD heterojunction and its application as a photocatalyst for the simultaneous oxidation of an azo dye and reduction of Cr(VI). Environ Sci Technol 42(10):3791–3796

Zhang H, Lv XJ, Li YM, Wang Y, Li J (2010a) P25-graphene composite as a high performance photocatalyst. ACS Nano 4(1):380–386

Zhang LJ, Zheng R, Li S, Liu BK, Wang DJ, Wang LL, Xie TF (2014a) Enhanced photocatalytic H_2 generation on cadmium sulfide nanorods with cobalt hydroxide as cocatalyst and insights into their photogenerated charge transfer properties. ACS Appl Mater Interfaces 6(16):13406–13412

Zhang J, Bang JH, Tang C, Kamat PV (2010b) Tailored TiO_2-$SrTiO_3$ heterostructure nanotube arrays for improved photoelectrochemical performance. ACS Nano 4(1):387–395

Zhang N, Shi JW, Mao SS, Guo LJ (2014b) Co_3O_4 quantum dots: reverse micelle synthesis and visible-light-driven photocatalytic overall water splitting. Chem Commun 50(16):2002–2004

Zhou X, Jin J, Zhu XJ, Huang J, Yu JG, Wong WY, Wong WK (2016) New $Co(OH)_2$/CdS nanowires for efficient visible light photocatalytic hydrogen production. J Mater Chem A 4(14):5282–5287